# Deformation and slip systems of $CaCl_2$-type $MnO_2$ under high pressure

HPSTAR 1430-2022

Binbin Yue,[1,*] Matthias Krug,[2] Carmen Sanchez-Valle,[2] Sébastien Merkel,[3,†] and Fang Hong[4,5,6,‡]

[1]*Center for High Pressure Science & Technology Advanced Research, 10 East Xibeiwang Road, Haidian, Beijing 100094, China*

[2]*Institute for Mineralogy, University of Münster, 48149 Münster, Germany*

[3]*Univ. Lille, CNRS, INRAE, Centrale Lille, UMR 8207 - UMET - Unité Matériaux et Transformations, F-59000 Lille, France*

[4]*Beijing National Laboratory for Condensed Matter Physics, Institute of Physics, Chinese Academy of Sciences, Beijing 100190, China*

[5]*School of Physical Sciences, University of Chinese Academy of Sciences, Beijing 100190, China*

[6]*Songshan Lake Materials Laboratory, Dongguan, Guangdong 523808, China*

(Received 14 December 2021; accepted 15 April 2022; published 3 May 2022)

Many nonmetals and metal dioxides $MO_2$, including the dense form of $SiO_2$ stishovite, crystalize in a rutile structure at low pressure and transform to a denser $CaCl_2$ structure under high pressure. Structures and transformations in $MO_2$ dioxides hence serve as an archetype for applications in materials science and inside the Earth and terrestrial planets. Despite its significance, however, the deformation behavior of $MO_2$ compounds in the $CaCl_2$ structure is very poorly constrained. Here we use radial x-ray diffraction in a diamond-anvil cell and study $MnO_2$ as a representative system of the $MO_2$ family. We identify the dominant slip systems and constrain texture evolution in $CaCl_2$-structured phases. After phase transition to a $CaCl_2$ structure above 3.5 GPa, the dominant (010)[100] and secondary {110}[001] and {011}[0-11] slip systems induce a 121 texture in compression. Further compression increases the activity of the {011}⟨0-11⟩ slip system, with an enhanced 001 texture at ∼50 GPa. During pressure release, the 001 texture becomes dominant over the original 121 texture. This clearly demonstrates the effect of pressure on the deformation behavior and slip systems of $CaCl_2$-structured dioxides. Finally, $MnO_2$ transforms back to a rutile structure upon pressure release, with a significant orientation memory, highlighting the martensitic nature of the $CaCl_2$ to rutile structural transformation. These findings provide key guidance regarding the plasticity of $CaCl_2$-structured dioxides, with implications in materials and Earth and planetary science.

DOI: 10.1103/PhysRevMaterials.6.053603

## I. INTRODUCTION

Many dioxides $MO_2$, where $M$ includes Si, Ge, Ru, Ti, Sn, Cr, Mn, etc., can crystalize in rutile structure (space group 136, $P4_2/mnm$). These compounds have attracted special attention due to their geophysical and technological relevance and, in the past several decades, numerous studies have been dedicated to identify their polymorphs and phase transition mechanisms under high pressure [1–9]. Under pressure, most rutile-structured $MO_2$ will transform to a $CaCl_2$ structure (space group 58, $Pnnm$). In Earth sciences, the rutile-to-$CaCl_2$ structural transformation in $SiO_2$ is proposed to be related to a seismic discontinuity at around 1200 km depth in the Earth's mantle [10]. In materials science, $MO_2$ compounds are promising materials in a wide range of fields, such as catalysis, battery electrodes, refractory, and thermoelectric devices [11–13]. For example, $MnO_2$ has attracted quite a lot of interest since it is an abundant, environment-friendly and relatively cheap material used in the fields of electrochemistry [12], magnetism [14] and catalysis [15].

Most of the previous studies mainly focused on the effect of pressure on the crystal structure of $MO_2$ compounds [2–6,16,17]. Other studies have investigated their elastic properties under pressure [7,18,19]. Their plastic deformation behavior, however, is much less studied, especially for the high-pressure $CaCl_2$ structures. As one kind of technological materials, the plastic deformation and the lattice-preferred orientation (LPO), or texture, formed in $MO_2$ compounds may have profound implications for their performances and applications [20]. In Earth science, LPO of rutile-structured stishovite $SiO_2$ and its high-pressure polymorph may contribute to seismic anomalies in the deep mantle [21], and knowledge of their deformation mechanism and their dependence on pressure would shed light on understanding the subduction of quartz-bearing crustal rocks into the mantle [22].

Previously, the plasticity of rutile-structured stishovite has been heavily studied by transmission electron microscopy (TEM) [23,24], radial x-ray diffraction in a diamond-anvil cell [22,25], and D-DIA apparatus [26]. Experiments on quenched stishovite [23,24], high-pressure deformed samples at room [22] and high temperature [26] lead to different dominant slip systems. In contrast, little is known about the deformation behavior of the $CaCl_2$-type phase, despite its relevance in understanding deep mantle dynamics below depths of 1000 km. This is due to the fact that stishovite transforms to a $CaCl_2$

*yuebb@hpstar.ac.cn

†sebastien.merkel@univ-lille.fr

‡hongfang@iphy.ac.cn

 ©2022 American Physical Society

structure above ∼50 GPa in pure $SiO_2$, and studies on the deformation behavior of this poststishovite phase are hence experimentally challenging. In contrast, $MnO_2$ transforms from a rutile structure to a $CaCl_2$ structure at much lower pressure (around or lower than 4 GPa [2,27]) as compared with $SiO_2$. Thus it can serve as a model system to study the deformation behavior of high-pressure dioxides, which is not only relevant for understanding and modeling the dynamics of the Earth´s interior, but has also implications in materials science for the general understanding of plasticity in $CaCl_2$-structured oxides.

Here, via *in situ* radial x-ray diffraction techniques in a diamond-anvil cell, we successfully revealed the deformation texture evolution in the $CaCl_2$-type phase of $MnO_2$ up to ∼50 GPa. The dislocation types that are dominant at different compression and decompression stages have also been identified successfully. The results clearly demonstrate the effect of pressure on the deformation behavior and slip systems of $CaCl_2$-structured dioxides.

## II. METHODS

### A. Experiments

The high-pressure radial x-ray diffraction experiments were conducted at room temperature at the BL04 beamline of ALBA Synchrotron, Spain. We used a panoramic diamond-anvil cell with a large side opening. Boron epoxy inserted into Kapton ring was used as an x-ray-transparent gasket. Polycrystalline $MnO_2$ was loaded into a 60-$\mu$m-diameter hole, along with a piece of Pt foil to serve as pressure marker. No pressure medium was used to maximize the deviatoric stress. A monochromatic x-ray beam of wavelength 0.4246 Å was focused onto the sample with a square-shaped beam of 15 × 15 $\mu m^2$. Instrument parameters, such as sample-to-detector distance, beam center, and detector tilt, were calibrated using a $LaB_6$ standard prior to the experiment.

Complementary measurements were also performed in axial geometry and under hydrostatic conditions at the BL15U beamline of SSRF, China. In this experiment, a stainless-steel gasket with a 100-$\mu$m sample chamber was used. Powder $MnO_2$ was prepressed to a thin foil, and a piece of it was loaded in the sample hole together with a ruby sphere and a small piece of Cu foil as pressure marker. Silicon oil was used as a pressure medium. The wavelength of the monochromatic x ray was 0.6199 Å with a beam size of around 2.2 × 3.0 $\mu$m (H × V). Instrument parameters were calibrated using a $CeO_2$ standard prior to the experiment.

### B. Radial x-ray diffraction data analysis

The Debye rings were unrolled to better present variations in both peak position and intensity. Diffraction images were then integrated over 5º increments of azimuthal arcs in Fit2d, resulting in 72 spectra for each image [28]. Then they were quantitatively analyzed in MAUD (Materials Analysis Using Diffraction) software [29] for hydrostatic cell parameters, phase proportions, textures, grain sizes, stress, and microstrains (heterogeneous strains). Data were fitted using rutile or $CaCl_2$-type structures at different pressure points. For the determination of crystallite size and microstrain, Popa line broadening with a Popa rules size-strain model was used [30]. The variations in peak positions with azimuthal angle are due to elastic strains in the sample grains in response to the macroscopic differential stress. In addition to elastic strain, the imposed differential stress also imposes plastic strain, which can lead to texture, manifested as variations in peak intensity with azimuth in diffraction patterns. The value of differential stress $t$ was refined using literature values of the Young's modulus $E$ and the Poisson ratio $\nu$ of $MnO_2$ at ambient conditions [31] via the triaxial stress isotropic E strain model in MAUD. Then we calculated $t/G = 2t\ (1+\nu)/\mathrm{E}$, which is independent of the choice of $E$ and $\nu$. Crystallographic textures were fitted using the entropy-modified Williams-Imhof-Matthies-Vinel (E-WIMV) algorithm [32] with an orientation distribution function (ODF) resolution of 15º and assuming cylindrical symmetry about the compression direction. The ODF was subsequently smoothed with a 7.5º Gauss filter to remove artifacts from the ODF resolution in BEARTEX [33]. Finally, we generated inverse pole figures (IPFs) that show the relationship between crystallographic directions of crystallites to the compression direction. Pole densities are given in multiples of a random distribution (m.r.d.), where m.r.d. = 1 corresponds to a random distribution and an m.r.d. of infinity corresponds to a single-crystal texture.

## III. RESULTS AND DISCUSSION

### A. Rutile-to-$CaCl_2$ phase transformation

Figure 1 shows the radial diffraction patterns of $MnO_2$ under nonhydrostatic compression and decompression. It can be clearly seen that at 1.9 GPa, a pure tetragonal phase is present and diffraction lines are indicating almost zero stress and lattice strain [Fig. 1(a)]. The pattern remains unchanged at 3.5 GPa. At 8.6 GPa, a new peak appears at around $2\theta = 10.8^\circ$, indicating that the phase transition has occurred [Fig. 1(g)]. This is confirmed with the hydrostatic axial diffraction measurements in which the phase transition is observed between 3.4 and 8.6 GPa [Fig. 2(a)]. The highest pressure reached is around 50 GPa, and no further phase transition can be observed in this range [see Figs. 1(b)–1(e) and 1(g)]. Haines *et al.* claimed a rutile-to-$CaCl_2$ phase transition in $MnO_2$ between 0.3 and 1.9 GPa with the splitting of the 200 reflection and broadening of the 101 and 211 reflections [2], but no raw data was given between 0.3 and 7.3 GPa. More recently, Curetti *et al.* carried out a delicate single-crystal x-ray diffraction experiment on $MnO_2$ and found that it underwent the rutile-to-$CaCl_2$ phase transition at around 4.05 GPa [27]. In our work, diffraction patterns collected from both axial geometry and hydrostatic condition [Fig. 2(a)] and radial geometry under nonhydrostatic condition [Fig. 1(g)] show no obvious changes below around 3.5 GPa. There was obvious splitting of 101 at higher pressure, indicating that the phase transition has occurred. This agrees well with the transition pressure proposed by Curetti *et al.* [27]. During decompression, the sample returned to the low-pressure rutile-type phase at around 2.8 GPa both under static and nonhydrostatic conditions [Figs. 1(f), 1(h), and 2(b)].

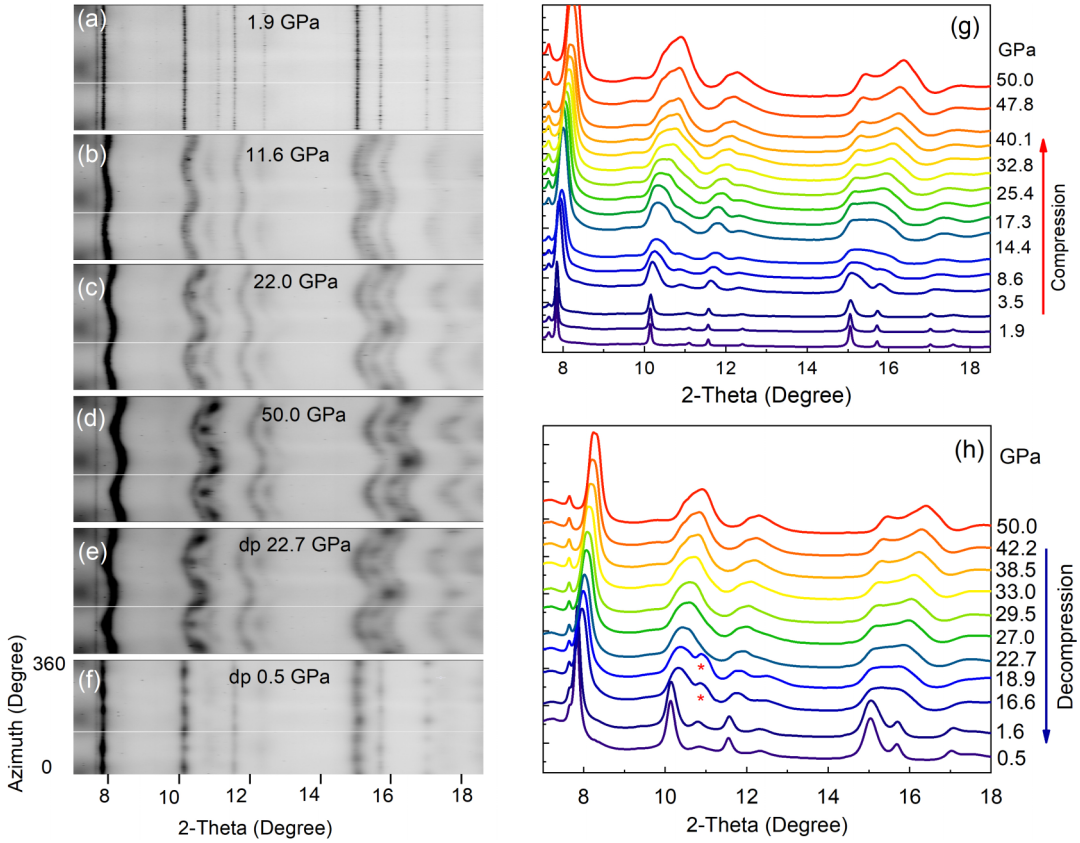


FIG. 1. Radial x-ray diffraction patterns of $MnO_2$. (a)–(f) Unrolled diffraction images showing stress and texture information at different pressure points during both compression and decompression. Analyzed diffraction patterns during compression (g) and decompression (h). The small peak at $2\theta = 7.6^\circ$ in (g) and (h) which does not move during the whole compression and decompression range is a signal from the gasket. Red stars in (h) indicate peaks from Pt. The x-ray wavelength is 0.4246 Å.

### B. Cell parameters and equation of state of $CaCl_2$-structured $MnO_2$

Figure 3 shows the hydrostatic lattice parameters and volume changes of both tetragonal rutile-type and orthorhombic $CaCl_2$-type phases with pressure obtained via radial diffraction. At 1.9 GPa, the lattice parameters are determined to be $a = 4.3927(1)$ and $c = 2.8688(3)$ Å. After phase transition, $a$ of the low-pressure rutile-type phase splits into $a$ and $b$ of the high-pressure $CaCl_2$-type phase. The value of $a$ slightly increases with pressure up to 17 GPa and then decreases, while $b$ decreases much faster than the other two lattice parameters. The $p$-$V$ data for the orthorhombic phase is fitted using a Birch-Murnaghan equation of state (EOS) with a fixed $K_0'$ of 4. A bulk modulus of 229 ± 6 GPa is obtained with $V_0 = 56.24 \pm 0.12$ Å$^3$. The hydrostatic axial diffraction data have also been refined, and results are shown in Figs. 2(c) and 2(d). Both lattice parameters and volume show a similar trend as those of the nonhydrostatic measurements. Third-order Birch-Murnaghan EOS fitting on the hydrostatic data yields a bulk modulus of 213 ± 19 GPa with a first pressure derivative $K_0' = 3.9 \pm 0.9$ and $V_0 = 55.79 \pm 0.18$ Å$^3$. Results of these two sets of measurements agree with each other and are also consistent with previous results on $MnO_2$ [2].

### C. Stress and texture

The stress state in a polycrystalline sample under uniaxial compression in the diamond-anvil cell can be described by a maximum stress along the cell loading axis $\sigma_3$ and a minimum stress in the radial direction $\sigma_1$. The difference between $\sigma_3$ and $\sigma_1$ is termed the differential stress $t$. The ratio of $t$ to shear modulus $G$ is a very useful parameter to compare different materials. The value of $t/G$ as a function of pressure of both phases is plotted in Fig. 3(c). For the low-pressure rutile-type phase, $t/G$ is quite low, which is consistent with the straight diffraction lines at 1.9 GPa [Fig. 1(a)]. The $t/G$ parameter increases dramatically during and after phase transition to a $CaCl_2$ structure, reaches ~0.015 at $P = 15$ GPa and remains around 0.02 up to $P = 50$ GPa. Such values for $t/G$ are similar to those of $SiO_2$ in the same pressure range [25]. The $t/G$ values below 3.5 GPa are very small, close to 0, indicating that the rutile-type phase was compressed under quasihydrostatic conditions and that plastic deformation of the sample starts to develop after the phase transition. Thus the low-pressure phase should have no influence on the deformation texture of the high-pressure $CaCl_2$-type phase.

Texture information of $MnO_2$ under high pressure was extracted from the MAUD refinement. IPFs of the compression

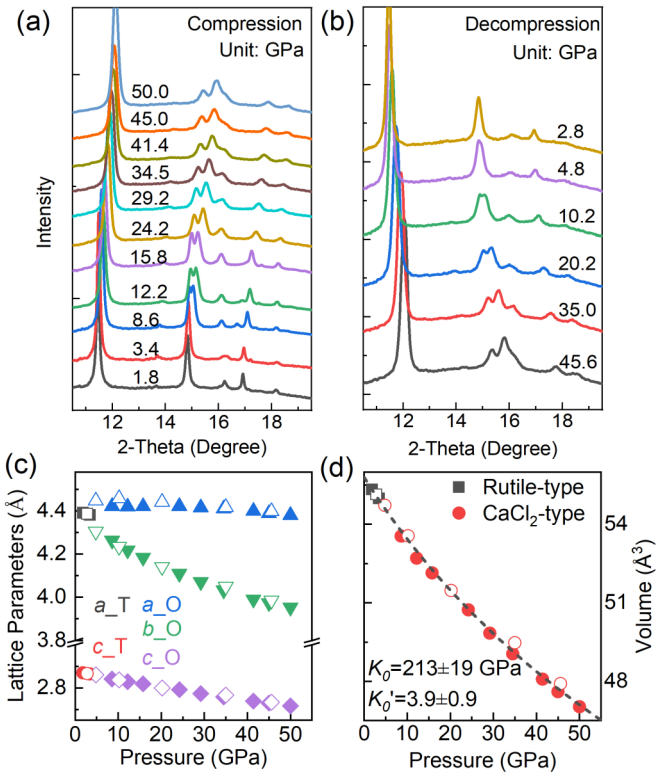


FIG. 2. X-ray diffraction results in axial geometry for hydrostatically compressed $MnO_2$. Integrated patterns of $MnO_2$ under (a) compression and (b) decompression. Lattice parameters (c) and volume (d) as a function of pressure. Solid symbols refer to points obtained upon compression and open symbols to those obtained on decompression. Dashed line in (d) is the third-order Birch-Murnaghan EOS fitting result. X-ray wavelength is 0.6199 Å.

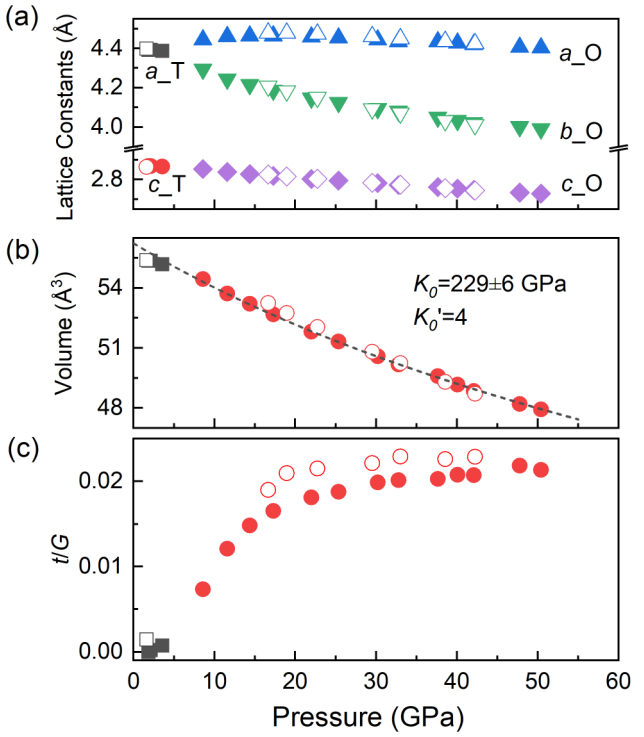


FIG. 3. Lattice parameters (a), volume (b), and $t/G$ (c) of $MnO_2$ as a function of pressure. Solid symbols refer to points obtained upon compression and open symbols to those obtained on decompression. In (b) and (c), the square and circle correspond to tetragonal (rutile-type) and orthorhombic ($CaCl_2$-type) phases, respectively. Dashed line in (b) is the EOS fitting result.

direction are used to show its evolution with pressure (Fig. 4). The low-pressure rutile-type phase shows a nearly random texture. The $CaCl_2$-type phase first develops a 121 texture at about 11.6 GPa and a second maximum at 001 at 17.3 GPa. The texture strength increases with pressure upon further compression to 50 GPa, with the largest intensity at 121 in the IPF. Interestingly, during decompression the IPF maximum moves from 121 to 001. When pressure is released to 1.6 GPa, $MnO_2$ transforms back to the original rutile-type phase with a main 001 texture and a secondary maximum at 211.

The texture development in $MnO_2$ can also clearly be observed in pole figures (Fig. 5). The 121 pole figure shows a maximum at its center at 11.6 GPa, indicating that the (121) planes of the $CaCl_2$-type phase are perpendicular to the compression direction. The 001 pole figure also develops a maximum at the center under higher pressure and becomes stronger than that of the 121 poles during decompression. During the $CaCl_2$ to rutile structural transition, the 001 pole of the $CaCl_2$ type becomes the 001 pole of the rutile type, while the 211 and 121 poles of the $CaCl_2$ type merge and become the 211 of the rutile type. Pole figures clearly show that the texture of the rutile-type phase is inherited from the $CaCl_2$-type phase, an indication of the martensitic nature of this phase transition.

### D. Deformation texture modeling in the $CaCl_2$-type structure

Deformation textures in the $CaCl_2$-type phase of $MnO_2$ were modeled using the Los Alamos viscoplastic self-consistent code (VPSC) [34]. VPSC simulations treat each grain as an inclusion in a homogeneous but anisotropic medium that has the average properties of the polycrystal. In agreement with observations (Fig. 4), we assumed a random starting texture. The deformation geometry was defined as uniaxial compression. Modeling was performed for a 3000-grains aggregate with 100 incremental steps up to a maximum strain of 15% or 30%, corresponding to different pressure points.

To our knowledge, slip systems in $CaCl_2$ structured dioxides (i.e., $MnO_2$, $SiO_2$, or $GeO_2$) have not been investigated yet since the samples cannot be quenched. For the modeling, we therefore used slip systems which were identified in isostructural materials [35,36] (see Table S1 in Supplemental Material [37]). Additionally, we used slip systems that are expected to be active in materials with rutile structure [38,39]. Various combinations of slip systems with various critical resolved shear stresses (CRSS) were tested. Our optimized results show that the combination of {110}[001], (010)[100], and {011}⟨0-11⟩ match the experimental results best [Fig. 6(a), Table I]. While both {110}[001] and (010)[100] are reported from both rutile-type structured materials and isostructural materials, {011}⟨0-11⟩ was only reported for rutile.

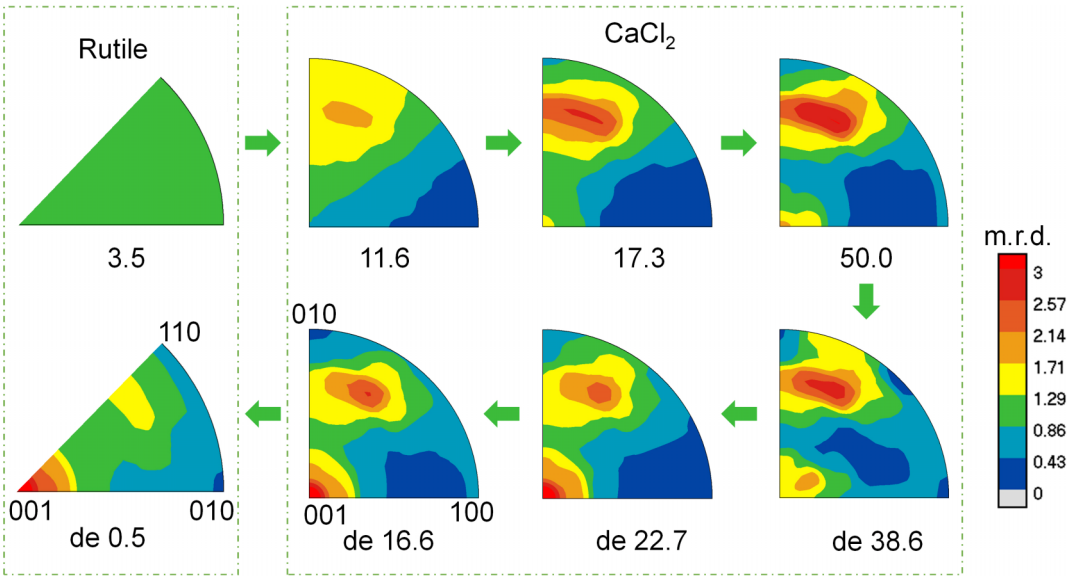


FIG. 4. Inverse pole figures of the compression direction showing the texture evolution in $MnO_2$ during compression and decompression. Pressure unit: GPa, *de* indicates decompression. Pole densities are measured in multiples of a random distribution (m.r.d.), where 1 m.r.d. represents random texture. Equal area projections.

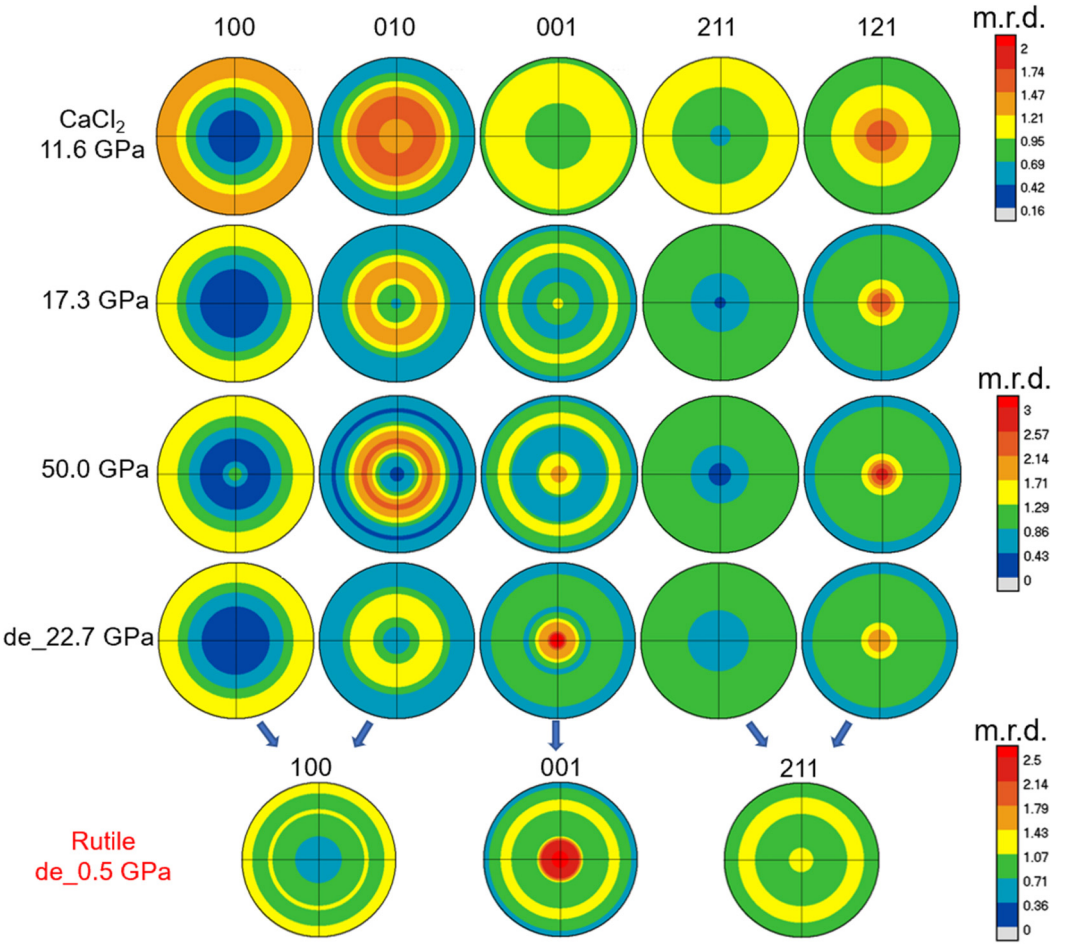


FIG. 5. Pole figures showing texture development in $CaCl_2$-type phase during both compression and decompression, and the texture inheritance during phase transition back to rutile phase. The viewed crystallographic lattice plane normal is indicated above each pole figure. The compression direction lies in the center of the pole figure, while the axis perpendicular to the compression direction lies in the peripheral. Equal area projection.

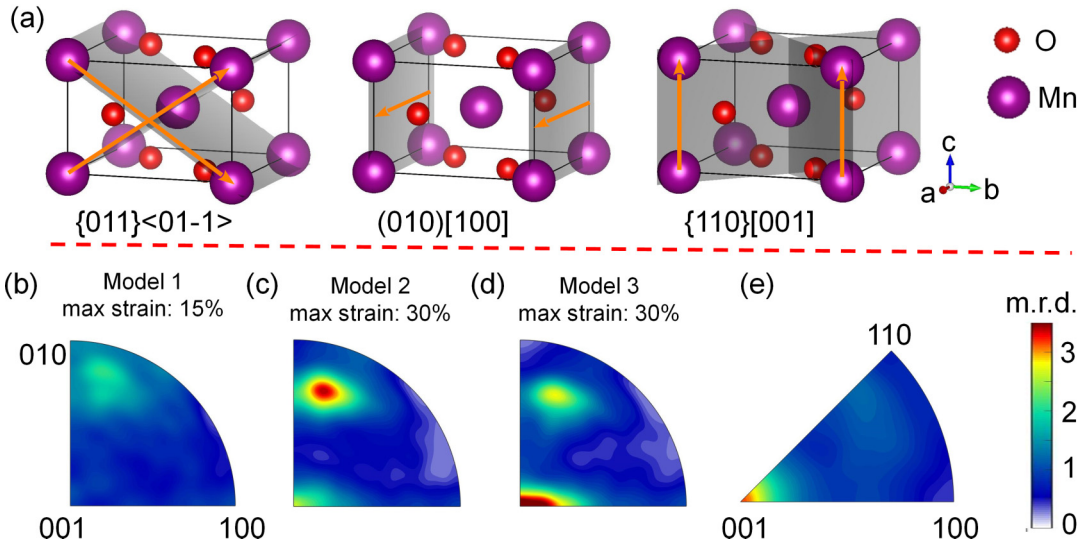


FIG. 6. Theoretical modeling texture results. (a) Slip systems used for VPSC modeling for $CaCl_2$-type phase. (b)–(d) VPSC modeling texture results corresponding to Table I, model 1 to model 3. (e) Modeled transformation texture of quenched rutile phase.

Upon compression to 11.6 GPa, the $CaCl_2$ type of $MnO_2$ phase develops a 121 maximum in the IPF, which is best reproduced by model 1 with dominant slip on (010)[100], with a plastic activity of 61.8%, in addition to slip on {110}[001] and {011}⟨0-11⟩ [Fig. 6(b)]. Model 2, with 45% and 41% plastic activity on (010)[100] and {011}⟨0-11⟩, respectively, leads to both the 121 and 001 IPF maxima, in agreement with measurements at 50 GPa [Figs. 4 and 6(c)]. Hence our results indicate a strong activity of (010)[100] in the early compression stage, followed by an increased activity of {011}⟨0-11⟩ at elevated pressure.

In stishovite, the elastic instability near the stishovite-$CaCl_2$ transition has long been an interesting topic, and many relevant experimental and theoretical works have been reported [19,23,25,40,41]. In these works the $(C_{11} - C_{12})/2$ constant, which reflects the resistance to deformation caused by shear stress along the [110] direction, vanishes close to the transition. Cordier *et al.* estimated that this softening would induce a change in the dominant slip systems at the vicinity of the transition with dominant easy slip on (1-10)[110] and (010)[100] replacing [001] slip as the $CaCl_2$ stability field is approached [23]. In our work it is clear that (010)[100] is the dominant slip system for the $CaCl_2$ phase (indexing for this slip system is consistent for both the rutile and the $CaCl_2$ structure) at the initial compression stage, which agrees well with the conclusion of Cordier *et al.* On the other hand, based on VPSC modeling, a dominant (1-10)[110] slip will lead to a 100 compression texture (see Fig. S2 in Supplemental Material [37]), which has not been observed in our experiments, indicating that the (1-10)[110] slip did not control the deformation texture in our experiment.

We observed an increase in texture intensity at 001 and a decrease in intensity at 121 when pressure is released to 16.6 GPa. We attempted to model this change of texture starting from that measured at 50 GPa and a tension geometry but failed to obtain satisfactory results. Moreover, the measured normalized stress [Fig. 3(c)] indicates that the sample remains in a compressive state during the release of hydrostatic pressure. This kind of phenomenon was previously reported in other systems. Miyagi *et al.*, for instance, observed that hcp iron developed a maximum at 11-20 during compression, while under decompression a 0001 maximum appeared together with the depletion of the 11-20 maximum due to the remaining compressive deviatoric stress state [42]. We hence modeled the decompression texture using an axial compression geometry. The experimental texture is well modeled using model 3, with 62% activity on {011}⟨0-11⟩ and 32% activity on (010)[100] [Fig. 6(d)].

TABLE I. VPSC calculation parameters. Each line is a simulation that best matches the corresponding experimental results. For each we report the CRSS (critical resolved shear stresses) of each slip system and their relative plastic activity (Act.). A maximum strain of 15% was used for model 1, and 30% was used for the other two. The corresponding compression textures are shown in Figs. 6(b)–6(d).

| | {110}[001] | | (010)[100] | | {011}⟨0-11⟩ | |
|---|---|---|---|---|---|---|
| | CRSS | Act. | CRSS | Act. | CRSS | Act. |
| Model 1 | 4 | 0.269 | 1 | 0.618 | 8 | 0.112 |
| Model 2 | 4 | 0.133 | 1 | 0.455 | 3 | 0.412 |
| Model 3 | 4 | 0.056 | 1 | 0.325 | 1.5 | 0.619 |

### E. Effect of pressure on slip system activity in $CaCl_2$-structured $MnO_2$

From the VPSC modeling results, it is quite clear that the initial high activity of the (010)[100] slip in addition to slip on {110}[001] and {011}⟨0-11⟩ leads to the 121 texture in $CaCl_2$-type $MnO_2$ shortly after the phase transition. The increasing activity of {011}⟨0-11⟩ leads to the 001 texture component under higher pressure up to 50 GPa. Finally, {011}⟨0-11⟩ becomes dominant during decompression with a strong 001

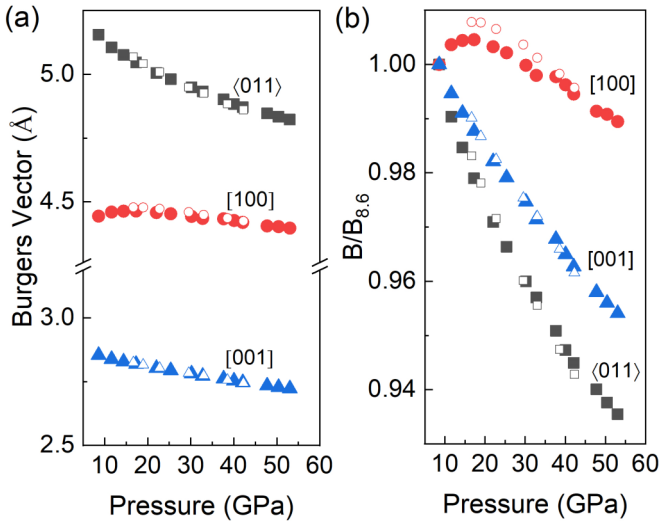


FIG. 7. Burgers vector of three slip systems used in VPSC. (a) Length of Burgers vector as a function of pressure. (b) Ratio of Burgers vector's length to that at 8.6 GPa. The length of the ⟨011⟩ Burgers vector decreases much faster with pressure than the other two. Solid symbols represent data obtained during compression and open symbols represent decompression data.

texture of $CaCl_2$-type $MnO_2$. The significant contribution of the {011}⟨0-11⟩ slip system is surprising, since its Burgers vector is comparably long [Figs. 6(a) and 7(a)], which is thought to be energetically unfavorable [43]. Note, however, that slip system with long Burgers vectors, ⟨100⟩ and ⟨101⟩, have also been reported for $SiO_2$ stishovite [44]. In addition, it is interesting to note that the length of the ⟨011⟩ Burgers vector decreases significantly with pressure relative to that of [100] [Fig. 7(b)]. We can hence speculate that the increased activity of the {011}⟨0-11⟩ slip at high pressure is related to changes in the relative Burgers vector's length.

### F. $CaCl_2$ to rutile phase transformation modeling

We observe a strong 001 texture together with a second maximum at 211 in the rutile phase upon pressure release. The transformation mechanism from a $CaCl_2$-type to a rutile-type structure is generally thought of as a displacive tetragonal distortion of the orthorhombic lattice. As a consequence, orientation relationships are expected between both phases: the crystallographic directions *a*, *b*, and *c* are identical in both structures. Using MTEX [45], we generated a set of 10 000 individual orientations from the ODF measured for the $CaCl_2$-type phase at 16.6 GPa during decompression, prior to the back-transformation to the rutile structure. The orientations were then converted to an ODF in the rutile crystal frame. The resulting IPF is shown in Fig. 6(e) with maxima at 001 and 211, as observed experimentally (Fig. 4). We can hence confirm that the phase transition is of martensitic nature, with orientation relationships between both phases. The texture measured in the rutile-type phase upon pressure release is entirely inherited from that of the $CaCl_2$-type phase prior to the transformation.

## IV. CONCLUSION

In this work, the deformation behavior of $CaCl_2$-type $MnO_2$ under high pressure has been investigated via *in situ* radial x-ray diffraction in a diamond-anvil cell. Thanks to the low phase transition pressure, pure deformation texture has been obtained for the $CaCl_2$-type phase, and we can identify the plastic mechanisms that control its plastic deformation. The dominant slip system (010)[100] with additional contributions of {110}[001] and {011}⟨0-11⟩ induced a 121 texture at the initial stage after phase transition, and the increased activity of {011}⟨0-11⟩ leads to another texture maximum at 001 at higher pressure. The increased activity of {011}⟨0-11⟩ at higher pressure is consistent with a pressure-induced shortening of the ⟨011⟩ Burgers vector relative to that of [100]. During decompression, the 001 texture strength keeps increasing, and VPSC modeling results show that the {011}⟨0-11⟩ slip becomes dominant. After pressure release, $MnO_2$ transform back to a rutile-type phase while inheriting the texture of the high-pressure phase, highlighting the martensitic nature of this phase transition.

Besides a general knowledge of the mechanical properties of $MO_2$ dioxides in the $CaCl_2$-type structure, the results have important implications for Earth and planetary sciences. Pure $SiO_2$ is an archetypical material for the silicate mineralogy of Earth and terrestrial planets and a relevant component of subducting slabs [46]. $SiO_2$ transforms from stishovite, in the rutile structure, to poststishovite in the $CaCl_2$ structure at ∼50 GPa in the pure phase and 28–42 GPa if Al is added to the structure [47]. Using $MnO_2$ as an analog for $SiO_2$ in the deep Earth mantle, our study suggests that (i) crystal orientations will be preserved across the phase transformation, and (ii) the plastic behavior of $SiO_2$, and hence crystal orientations, will change with the stishovite to poststishovite phase transformation and further evolve with depth. A change in $SiO_2$ crystal orientations will affect wave propagation in subducting slabs and, potentially, be related to ubiquitous observations of seismic scatters [48] and reflectors in the midmantle [49,50]. These observations are a marker for compositional heterogeneity at midmantle depths, and relating them to texture and crystal orientations could help with reconstructing the dynamics and history of this region.

## ACKNOWLEDGMENTS

This work is financially supported by the National Natural Science Foundation of China (Grants No. 12004014 and No. U1930401). Parts of the experiments were performed at MSPD beamline at the ALBA Synchrotron with the collaboration of ALBA staff Catalin Alexandru Popescu. The authors also acknowledge the use of BL15U at Shanghai Synchrotron Radiation Facilities. S.M. and M.K. acknowledge support from the bilateral ANR-DFG TIMEleSS project (ANR-17-CE31-0025; TH 1530/18-1, SA 2585/3-1, and SP1216/8-1), the bilateral PROCOPE-PPP program (Grants No. 40555PC and DAAD No. 57390184), and the Chevreul Institute. The Chevreul Institute is thanked for its help in the development of this work through the ARCHI-CM project supported by the Ministère de l'Enseignement Supérieur de la Recherche et de l'Innovation, the region Hauts-de-France, the ERDF program of the European Union, and the Métropole Européenne de Lille.

[1] D. Andrault, G. Fiquet, F. Guyot, and M. Hanfland, Science **282**, 720 (1998).

[2] J. Haines, J. M. Léger, and S. Hoyau, J. Phys. Chem. Solids **56**, 965 (1995).

[3] J. Haines and J. M. Léger, Phys. Rev. B **55**, 11144 (1997).

[4] J. Haines, J. M. Léger, C. Chateau, and A. S. Pereira, Phys. Chem. Miner. **27**, 575 (2000).

[5] B. R. Maddox, C. S. Yoo, D. Kasinathan, W. E. Pickett, and R. T. Scalettar, Phys. Rev. B **73**, 144111 (2006).

[6] R. A. Fischer, A. J. Campbell, B. A. Chidester, D. M. Reaman, E. C. Thompson, J. S. Pigott, V. B. Prakapenka, and J. S. Smith, Am. Mineral. **103**, 792 (2018).

[7] Z. Łodziana, K. Parlinski, and J. Hafner, Phys. Rev. B **63**, 134106 (2001).

[8] J. Haines, J. M. Léger, F. Gorelli, and M. Hanfland, Phys. Rev. Lett. **87**, 155503 (2001).

[9] H. T. Girao, P. Hermet, B. Masenelli, J. Haines, P. Mélinon, and D. Machon, Phys. Rev. Lett. **120**, 265702 (2018).

[10] Y. Tsuchida and T. Yagi, Nature (London) **340**, 217 (1989).

[11] K. Qi, B. Cheng, J. Yu, and W. Ho, Chin. J. Catal. **38**, 1936 (2017).

[12] X. Liu, J. Yi, K. Wu, Y. Jiang, Y. Liu, B. Zhao, W. Li, and J. Zhang, Nanotechnology **31**, 122001 (2020).

[13] S. Thébaud, C. Adessi, and G. Bouzerar, Phys. Rev. B **100**, 195202 (2019).

[14] M. Regulski, R. Przeniosło, I. Sosnowska, and J. U. Hoffmann, Phys. Rev. B **68**, 172401 (2003).

[15] X. Weng, Y. Long, W. Wang, M. Shao, and Z. Wu, Chin. J. Catal. **40**, 638 (2019).

[16] R. Wu and W. H. Weber, J. Phys.: Condens. Matter **12**, 6725 (2000).

[17] S. R. Shieh, A. Kubo, T. S. Duffy, V. B. Prakapenka, and G. Shen, Phys. Rev. B **73**, 014105 (2006).

[18] H. Hellwig, A. F. Goncharov, E. Gregoryanz, H.-k. Mao, and R. J. Hemley, Phys. Rev. B **67**, 174110 (2003).

[19] R. Yang and Z. Wu, Earth Planet. Sci. Lett. **404**, 14 (2014).

[20] U. Gesenhues, J. Phys. Chem. Solids **68**, 224 (2007).

[21] Y. Asahara, K. Hirose, Y. Ohishi, N. Hirao, H. Ozawa, and M. Murakami, Am. Mineral. **98**, 2053 (2013).

[22] P. M. Kaercher, E. Zepeda-Alarcon, V. B. Prakapenka, W. Kanitpanyacharoen, J. S. Smith, S. Sinogeikin, and H.-R. Wenk, Phys. Chem. Miner. **42**, 275 (2015).

[23] A. P. Cordier, A. D. Mainprice, and J. L. Mosenfelder, Eur. J. Mineral. **16**, 387 (2004).

[24] M. Texier and P. Cordier, Phys. Chem. Miner. **33**, 394 (2006).

[25] S. R. Shieh, T. S. Duffy, and B. Li, Phys. Rev. Lett. **89**, 255507 (2002).

[26] F. Xu, D. Yamazaki, N. Tsujino, and L. Guan, Phys. Earth Planet. Inter. **306**, 106546 (2020).

[27] N. Curetti, M. Merli, S. Capella, P. Benna, and A. Pavese, Phys. Chem. Miner. **46**, 987 (2019).

[28] A. P. Hammersley, S. O. Svensson, M. Hanfland, A. N. Fitch, and D. Hausermann, High Pressure Res. **14**, 235 (1996).

[29] L. Lutterotti, S. Matthies, H.-R. Wenk, A. S. Schultz, and J. W. Richardson, J. Appl. Phys. **81**, 594 (1997).

[30] N. C. Popa and D. Balzar, J. Appl. Crystallogr. **35**, 338 (2002).

[31] S. Ma, X. Ye, X. Jiang, W. Cen, W. Jiang, and H. Wang, J. Alloys Compd. **852**, 157007 (2021).

[32] D. Chateigner, L. Lutterotti, and M. Morales, in *International Tables for Crystallography* (John wiley & Sons, London, 2019), p. 555.

[33] H.-R. Wenk, S. Matthies, J. Donovan, and D. Chateigner, J. Appl. Crystallogr. **31**, 262 (1998).

[34] R. A. Lebensohn and C. N. Tomé, Acta Metall. Mater. **41**, 2611 (1993).

[35] A. Lefebvre, Bulletin de Minéralogie **105**, 347 (1982).

[36] A. Mussi, P. Cordier, and D. J. Frost, Eur. J. Mineral. **25**, 561 (2013).

[37] See Supplemental Material at http://link.aps.org/supplemental/10.1103/PhysRevMaterials.6.053603 for data processing and modeling details.

[38] K. H. G. Ashbee, R. E. Smallman, and G. V. Raynor, Proc. R. Soc. London, A **274**, 195 (1963).

[39] A. Péter, E. Fries, J. Janszky, and J. Castaing, Rev. Phys. Appl. **21**, 289 (1986).

[40] Y. Zhang, S. Fu, B. Wang, and J.-F. Lin, Phys. Rev. Lett. **126**, 025701 (2021).

[41] M. A. Carpenter, R. J. Hemley, and H.-k. Mao, J. Geophys. Res. Solid Earth **105**, 10807 (2000).

[42] L. Miyagi, M. Kunz, J. Knight, J. Nasiatka, M. Voltolini, and H.-R. Wenk, J. Appl. Phys. **104**, 103510 (2008).

[43] J. Friedel, in *Dislocations*, edited by J. Friedel (Pergamon, New York, 1964), p. 17.

[44] P. Cordier and T. G. Sharp, Phys. Chem. Miner. **25**, 548 (1998).

[45] D. Mainprice, F. Bachmann, R. Hielscher, H. Schaeben, G. E. Lloyd, D. R. Faulkner, E. Mariani, and J. Mecklenburgh, in *Rock Deformation from Field, Experiments and Theory: A Volume in Honour of Ernie Rutter* (Geological Society of London, Piccadilly London, 2016), p. 251.

[46] A. Ricolleau, J.-P. Perrillat, G. Fiquet, I. Daniel, J. Matas, A. Addad, N. Menguy, H. Cardon, M. Mezouar, and N. Guignot, J. Geophys. Res. Solid Earth **115**, B08202 (2010).

[47] C. Nisr, K. Leinenweber, V. Prakapenka, C. Prescher, S. Tkachev, and S.-H. D. Shim, J. Geophys. Res. Solid Earth **122**, 6972 (2017).

[48] S. Kaneshima, Phys. Earth Planet. Inter. **257**, 105 (2016).

[49] J. Jenkins, A. Deuss, and S. Cottaar, Earth Planet. Sci. Lett. **459**, 196 (2017).

[50] L. Waszek, N. C. Schmerr, and M. D. Ballmer, Nat. Commun. **9**, 385 (2018).